Propagation and Exposure Assessment of RIS-Shaped mmWave Fields in a Greenhouse

Felipe Oliveira Ribas, Günter Vermeeren, Thomas Zemen, *Senior Member, IEEE*, Milica Djordjevic, Hamed Radpour, *Graduate Student Member, IEEE*, and Wout Joseph

***Abstract*—Millimeter-wave (mmWave) links in greenhouses are challenged by dense vegetation, which blocks line-of-sight and produces scattering-dominated channels. We present a hybrid ray-tracing (RT) to full-wave finite-difference time-domain (FDTD) framework to jointly assess propagation and exposure at 26 GHz in a realistic tomato-greenhouse geometry. RT simulations (Sionna) were performed for 440 receiver (RX) locations and the dominant multipath components were mapped to a coherent multiplane-wave excitation in FDTD (Sim4Life) to compute absorbed metrics for a *Bombus terrestris* model (total absorbed power) and a human head phantom with absorbed power density averaged over 4 cm² (APD_{4cm^2}). For isotropic transmission, the mean coherent path gain of approximately −122 dB corresponds to a noise-limited regime, with insect absorbed power typically in the 10^{-14}–10^{-12} W range. With directional illumination, a reconfigurable intelligent surface (RIS) increases the mean coherent path gain by approximately 56.9 dB relative to the isotropic baseline and narrows the central 90% gain interval to approximately [−76, −50] dB and produces substantially stronger location-dependent optimized links; the resulting insect absorbed power is typically 10^{-10}–10^{-8} W and reaches 1.5×10^{-6} W under the strongest optimized RX condition. Human exposure remains below 10^{-4} W/m² in all scenarios, is confined to superficial tissues, and remains more than 53 dB below the international commission on non-ionizing radiation protection (ICNIRP) 2020 general-public local basic restriction. The results quantify the connectivity gains of RIS-assisted mmWave links in vegetation-dense layouts and the spatial variability of the corresponding optimized propagation and exposure conditions.**

***Index Terms*—electromagnetic field (EMF) exposure, finite-difference time-domain (FDTD), ray-tracing (RT), reconfigurable intelligent surface (RIS).**

I. Introduction

MILLIMETER-WAVE (mmWave) systems are increasingly considered for industrial and agricultural automation [1], [2]. Together with directional arrays, emerging field-shaping technologies, such as reconfigurable intelligent surfaces (RISs), can strongly modify the spatial distribution of the electromagnetic field. While this can restore coverage in blocked conditions, it also motivates exposure and compliance assessment because field control may create localized power-density hotspots depending on the configuration.

Greenhouses provide a challenging propagation environment for such systems. Dense vegetation and structural clutter attenuate and scatter mmWave signals, often eliminating line-of-sight (LoS) and producing highly variable multipath channels [3], [4], [5], [6]. RISs have been proposed to re-establish connectivity by engineering reflections when LoS is blocked, especially when combined with directional illumination [7]. RIS control has also been discussed as a means to reshape exposure by steering energy away from selected regions [8], [9], [10].

At mmWave frequencies, energy deposition in tissue is predominantly superficial [11]. For local exposures above 6 GHz, recent guidelines and standards define surface-related dosimetric and reference quantities, including absorbed and incident power density (APD/IPD), for human exposure assessment [12], [13], [14], [15], [16], [17]. Accordingly, APD_{4cm^2} is commonly used for human exposure evaluation and comparison with guideline-based limits [12], [14], [18], [19].

Full-wave simulations are routinely applied to quantify mmWave exposure for directive fields and anatomical models [18], [19], [20]. However, full-wave modeling of an entire deployment environment is generally computationally impractical. Hybrid ray-tracing (RT)-finite-difference time-domain (FDTD) methods address this limitation by separating the problem into an environment-scale propagation stage and a local full-wave stage. In this framework, RT efficiently characterizes the site-specific propagation channel, whereas FDTD resolves the interaction of the incident fields with the exposed body or object in the region where full-wave accuracy is required [21], [22], [23].

This principle has been applied to human exposure assessment by coupling RT-derived channel information to anatomical FDTD simulations for massive multiple-input multiple-output (MIMO) deployments and user-induced coupling [22], [24], [25]. In these studies, reliability was assessed through methodological verification, numerical-error and convergence analyses, sensitivity studies, and comparison with expected physical propagation behavior. The approach was subsequently applied to realistic indoor exposure assessment at 3.5 and 28 GHz, including absorbed power density at mmWave frequencies [26], and more recently extended to a hybrid RT/QuaDRiGa–FDTD workflow using a Huygens-box interface for realistic 28 GHz outdoor exposure assessment [23].

Related work also addresses compliance-oriented estimation of IPD at quasi-mmWave and mmWave frequencies [27], [28],

Received 26 February 2026; revised 15 June 2026; accepted 11 August 2026. *(Corresponding author: Felipe Oliveira Ribas.)*

Felipe Oliveira Ribas, Günter Vermeeren, and Wout Joseph are with the Department of Information Technology, WAVES, Ghent University/IMEC, 9052 Ghent, Belgium (e-mail: felipe.oliveiraribas@ugent.be).

Thomas Zemen, Milica Djordjevic, and Hamed Radpour are with the AIT Austrian Institute of Technology, 1210 Vienna, Austria.

Color versions of one or more figures in this article are available at https://doi.org/10.1109/TEMC.2026.3725464.

Digital Object Identifier 10.1109/TEMC.2026.3725464

[29], [30], uncertainty-aware exposure evaluation [31], and realistic indoor deployments combining propagation and dosimetry [25], [32], [33].

For insects, previous dosimetry studies have shown that absorbed power can increase substantially with frequency in the GHz-to-mmWave range [34], [35], [36]. At the same time, currently used exposure limits and reference quantities are defined for human protection, and insect-specific protection criteria are not established. Therefore, in the present work, the insect model is evaluated using total absorbed power as a dosimetric outcome rather than a compliance metric [12], [37].

Despite this progress, hybrid propagation-to-dosimetry studies in agricultural environments remain largely unexplored. Greenhouses introduce specific propagation challenges, including vegetation blockage, canopy-dependent attenuation, structural clutter, and uncertainty in plant geometry and material properties. Moreover, RIS-assisted field shaping has not yet been evaluated within this hybrid exposure framework. Previous hybrid RT–FDTD exposure studies have also focused primarily on human exposure, whereas absorbed power in small nonhuman organisms, such as insects, remains unaddressed. The present work extends the established hybrid methodology to jointly evaluate RIS-assisted propagation, human surface exposure, and insect absorbed power in a vegetation-dense greenhouse environment.

In this work, we combine greenhouse-scale RT with full-wave FDTD at 26 GHz to connect propagation and exposure in a realistic vegetation-dense layout. We 1) quantify link statistics across 440 locations for isotropic, RIS-assisted directional, and LoS reference illumination, 2) translate dominant multipath parameters into full-wave simulations to quantify exposure for both a human head phantom ($\mathrm{APD}_{4\mathrm{cm}^2}$, enabling comparison with guidelines) and a small-body model (total absorbed power), using a *Bombus terrestris* bumblebee as a representative pollinator commonly present in commercial tomato greenhouses, and 3) characterize upper bound, location-dependent propagation and exposure conditions using RIS configurations optimized for each receiver (RX).

II. Methods

A. Greenhouse Geometry and Material Modeling

A 3-D greenhouse environment was created in Blender v4.5.1. The geometry follows representative industrial layouts, spanning approximately 75 × 75 × 10 m and containing 22 tomato crop rows arranged symmetrically around a central corridor (see Fig. 1).

The vegetation was represented as a homogeneous effective medium.

B. RT Setup

All propagation simulations were run in Sionna RT v0.19.2 [38] at 26 GHz with 200 MHz bandwidth.

LoS propagation, specular reflection, diffuse scattering, diffraction, and RIS-assisted propagation were enabled. Transmission or refraction through scene objects was not included because it was not available as a separate propagation-path option in the Sionna RT v0.19.2 version used. The maximum path depth was set to 8, allowing up to eight propagation interactions per computed path.

Receivers were modeled as isotropic (1 × 1) in Sionna; therefore, reported path gains correspond to isotropic reception.

1) Transmitter (TX) Placement and Configuration: The TX, with a conducted power of 20 dBm (0.1 W), was placed at $(x, y, z) = (0, 0, 5)$ m at the greenhouse entrance [see Fig. 1(b)]. This position was selected to cover a range of propagation conditions across the RX grid rather than as the result of an optimization over alternative TX locations. The TX–RX distance ranges from 7.23 to 74.53 m. With the TX at a height of 5 m and the RXs at 2 m, the corresponding elevation angles range from approximately $-24.5°$ to $-2.3°$. The RX positions extend across both crop blocks and 22 crop-row indices, providing different azimuth directions and progressively greater vegetation blockage with distance from the greenhouse entrance.

Two operating modes were used as follows.

- Isotropic radiator: Omni-directional, vertically polarized.
- Directional TR 38.901 (standardized third generation partnership project (3GPP) TR 38.901 antenna radiation pattern [39]) 4 × 4 array: vertically polarized elements, 0.5λ spacing, beam-steered toward the active RIS.

The isotropic radiator has 0 dBi peak gain, whereas the 4 × 4 array combines the TR 38.901 element pattern (about 8 dBi peak) with a 16-element array factor (about 12 dB), yielding an approximate 20 dBi peak gain; thus, for the same conducted transmit power, the directional mode increases equivalent isotropically radiated power (EIRP) by roughly 20 dB relative to the isotropic case.

2) TX-at-RIS Upper Bound Reference: In addition to the baseline and RIS-assisted scenarios, we simulated a LoS upper bound reference to represent the best achievable channel gain in this greenhouse geometry when blockage is removed. In this reference, the same directional TX configuration (TR 38.901 4 × 4 array, vertical polarization, $P_{\mathrm{tx}} = 20$ dBm, and beam steering) was used, but the TX was placed at the RIS location (i.e., at the same coordinates and height as the RIS panel in each snapshot). The beam was then steered directly toward the active RX.

This LoS reference does not represent a practical deployment with many TXs, but provides a physically meaningful upper bound for the considered links. It serves as an upper bound benchmark to quantify the gap between RIS-assisted links and direct LoS illumination under identical TX settings.

This configuration is referred to as a LoS reference throughout this article, i.e., a direct-illumination upper bound obtained by collocating the TX with the RIS position.

3) RIS Placement and Electromagnetic Model: The RIS was implemented using Sionna RT's dedicated RIS class as one RIS device with a 30 × 30 unit-cell grid. The RIS is therefore not inserted into the scene as 900 separate metallic mesh objects. However, the unit cells are individually represented in the RIS calculation through their positions and programmed amplitude and phase values. Sionna constructs RIS-assisted TX–RIS–RX

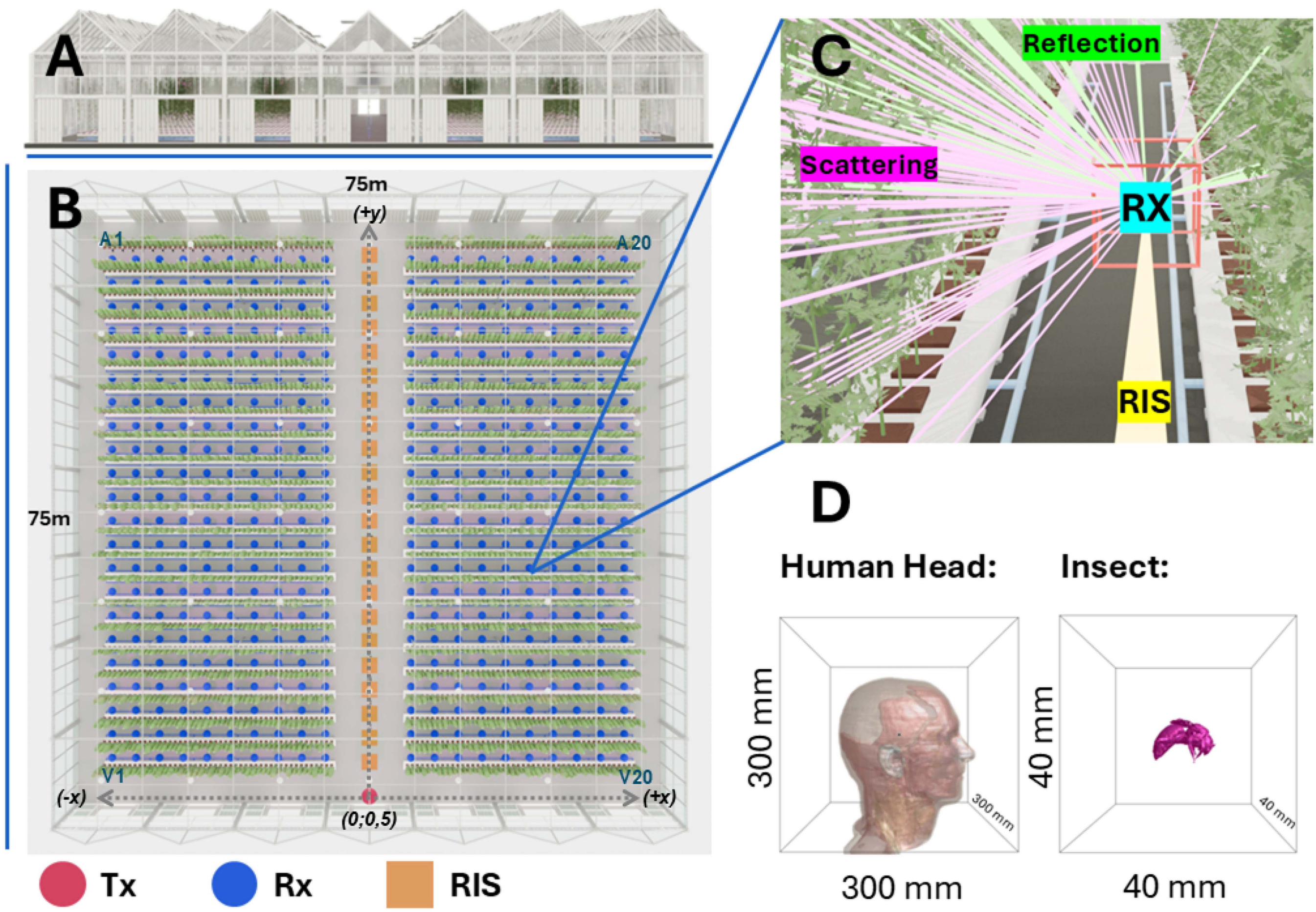

Fig. 1. Simulated greenhouse and exposure workflow. (a) Side view of the tomato greenhouse used for RT. (b) Top view of the 75 m $\times$ 75 m layout, showing the vegetation rows and central corridor. The coordinate origin is located at the transmitter (TX) position at the greenhouse entrance. The $+y$-direction follows the central corridor toward the greenhouse interior, while the $+x$-direction is transverse to the corridor; the z-axis is vertical. The TX is shown in red, the 440 RX positions in blue, with 20 RXs per crop-row index, and the 22 alternative RIS candidate positions in yellow. Only one RIS candidate position was active in each RT snapshot. (c) Example RX under RIS-assisted illumination, showing vegetation scattering and RIS reflection forming a coherent TX–RIS–RX path. (d) Full-wave phantoms and excitation domains: human head (300 mm cube) and *Bombus terrestris* worker (40 mm cube) under plane-wave incidence. .

components through the individual cell positions, and the resulting cell-level contributions are combined coherently in the calculation of the reradiated field.

With $\lambda/2$ unit-cell spacing at 26 GHz, the resulting aperture is 17.3 cm $\times$ 17.3 cm.

The unit cells follow Sionna's radiation mode 1, with ideal phase-only reflection, unit amplitude, and no mutual coupling; nonideal reflection losses and distortions are therefore neglected [40], [41]. The RIS height was set to 4 m, above the vegetation adjacent to the central corridor.

The RIS was configured through a combination of mechanical orientation and electronic phase control, and was reconfigured independently for each evaluated RX position (one simulation snapshot per RX). For every RX location, the RIS was mechanically rotated so that its surface normal aligned with the angular bisector of the TX$\rightarrow$RIS and RIS$\rightarrow$RX directions. The element phases were then computed deterministically from the known TX/RX/RIS geometry using a closed-form phase-gradient model (ideal lens steering the reflected field toward that RX assuming perfect knowledge of the RX position).

This per-RX mechanical orientation and phase optimization represents an idealized upper bound for the considered RIS-assisted configurations. It maximizes coherent TX–RIS–RX coupling and field localization within the modeled RIS framework, whereas the direct LoS reference remains the direct-illumination upper bound benchmark.

Only one RIS panel was active in each simulation snapshot. The 22 yellow markers in Fig. 1(b) represent alternative candidate positions for this panel along the central corridor, rather than 22 simultaneously active RISs. For each RX, only the candidate position associated with the corresponding crop-row index was activated and configured toward that RX. The candidate positions were located at a height of 4 m. Each candidate position was associated with 20 RX locations, with ten RXs on each side of the corridor, giving 440 RX positions in total. The directional TX beam was steered toward the active RIS candidate position.

The RIS configurations are denoted according to their mechanical orientation and electronic phase control. RIS (M-RX/P-RX) denotes the optimized configuration used in the exposure analysis, in which both the mechanical orientation and the phase profile were recalculated separately for each RX. RIS (M-Fix/P-RX) denotes a constrained configuration in which one mechanical orientation was retained within each row-side group, while the phase profile was recalculated for each target RX. In RIS (M-Fix/P-Fix), both the mechanical orientation and the phase profile were fixed toward the farthest RX in the corresponding row-side group.

In all configurations, the directional TX beam was steered toward the active RIS candidate position rather than directly toward the individual RX. Because each candidate position was associated with 20 RX locations, the TX beam direction remained unchanged for all RXs associated with that candidate position.

4) Receiver Distribution: A total of 440 RX positions were distributed across 22 crop-row indices. For each index, 10 RX positions were placed on each side of the central corridor, giving 20 RX positions per index. The RXs were placed at a height of 2 m, with 3 m spacing between consecutive positions along each row.

Rows were labeled A–V in increasing order of distance from the TX, with row A closest to the TX and row V farthest away. Within each row, the 20 RX positions were numbered from 1 to 20 when viewed from the TX. Positions 1–10 were located on the left side of the central corridor, and positions 11–20 on the right side.

In the modeled greenhouse layout, the RIS–RX separation spans 5.61–32.62 m, while TX–RX distances range from 7.23 to 74.53 m.

C. Bounding Assumptions and Worst-Case Interpretation

To bound field localization within the modeled RIS framework, the RIS configuration was optimized per RX (snapshot-by-snapshot) to maximize coherent TX–RIS–RX coupling. The resulting exposure levels represent an idealized upper bound for the considered RIS configurations, rather than an upper bound relative to other passive or active reflecting solutions. Additional bounding and modeling assumptions include ideal phase-only RIS reflection with unit amplitude, homogeneous vegetation dielectric parameters, and the local representation of each retained RT component as an equivalent plane wave at the phantom location.

D. Phantoms: Geometry, Materials, and Resolution

Each RX position defines one simulation snapshot for exposure: the phantom domain was centered at the RX location and illuminated using an equivalent multiplane-wave excitation derived from the dominant RT multipath components for that RX.

1) Insect: A *Bombus terrestris* worker was reconstructed from a high-resolution photogrammetry model [42] [see Fig. 1(d)]. The phantom preserves the external morphology of the photogrammetry model but was treated as homogeneous because segmented internal anatomy and species-specific dielectric data at 26 GHz are not currently available. Measured honeybee dielectric properties were used as the closest available proxy, with nominal values of $\varepsilon_r = 6.70$ and $\sigma = 9.4$ S/m [43].

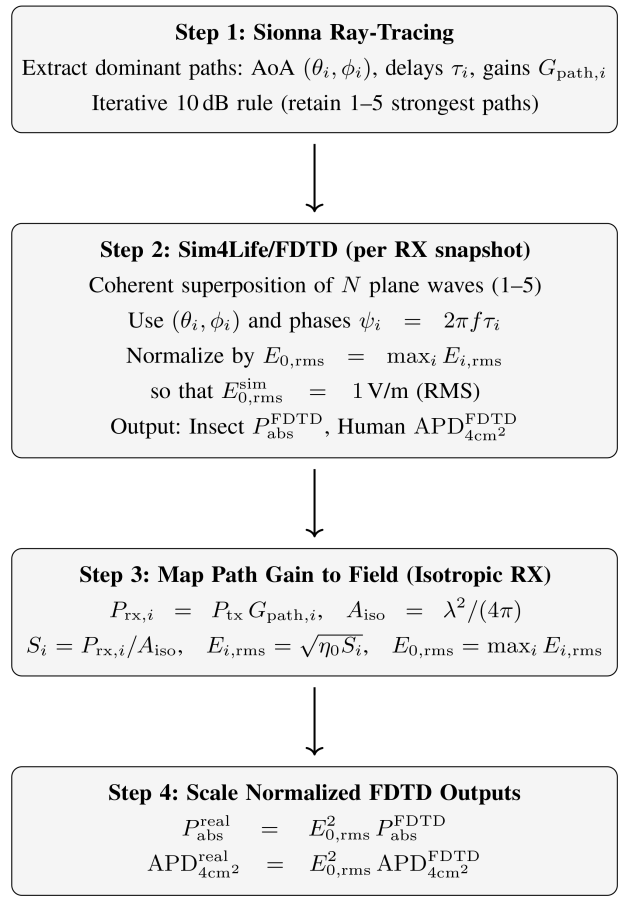

Fig. 2. Workflow of the RT to full-wave exposure pipeline. Dominant paths define a coherent multiplane-wave excitation; normalized FDTD outputs are scaled to physical absorbed metrics using E_0^2.

The sensitivity to the assumed dielectric properties was evaluated by varying ε_r and σ independently by $\pm 50\%$ around their nominal values, resulting in nine parameter combinations. Across these cases, P_{abs} ranged from 1.67×10^{-8} to 2.21×10^{-8} W, compared with 2.04×10^{-8} W for the nominal case. This corresponds to differences from -18.1% to +8.3% relative to the nominal result. This analysis quantifies sensitivity to the dielectric properties only; the uncertainty introduced by the homogeneous representation of the internal anatomy was not evaluated separately.

The phantom was placed in a $40 \times 40 \times 40$ mm^3 source region [see Fig. 1(d)]. Insect FDTD simulations used a spatial resolution of $\Delta = 0.08$ mm.

For the insect model, exposure was quantified as total absorbed power P_{abs}, since the 4 cm^2 spatial-averaging area used for human APD metrics is not meaningful at insect scale.

2) Human: The human phantom was based on the IXI Heads V1.0 model provided by the IT'IS Foundation [44]. Frequency-dependent dielectric properties for each tissue were assigned according to the IT'IS tissue parameter database. For the human head, $\mathrm{APD}_{4\mathrm{cm}^2}$ was computed as a surface-averaged absorbed power density over 4 cm^2 on the exposed skin region to enable comparison with established exposure limits at mmWave frequencies.

For each human-head snapshot, the reported $\mathrm{APD}_{4\mathrm{cm}^2}$ corresponds to the peak absorbed power density averaged over a contiguous 4 cm^2 skin-surface area, as computed in Sim4Life using the same anatomical orientation across all snapshots.

The human head was simulated in a dedicated source region of $300 \times 300 \times 300\,\mathrm{mm}^3$ [see Fig. 1(d)]. Human FDTD simulations used a spatial resolution of $\Delta = 1$ mm.

This head-only modeling choice is consistent with recent mmWave dosimetry studies that evaluate local APD/IPD-related quantities on anatomical head or nonplanar body models, where the focus is on local surface exposure above 6 GHz rather than whole-body absorption [14], [15], [18], [19], [20]. In the present work, the IXI head serves as a representative anatomically realistic nonplanar human surface for local dosimetric comparison while keeping the RT-to-FDTD workflow computationally tractable across all simulation snapshots.

The FDTD domains were terminated on all six sides using Sim4Life absorbing boundaries with the uniaxial perfectly matched layer (UPML)/convolutional perfectly matched layer (CPML) method and medium boundary strength. Time steps were selected automatically from the final nonuniform grids according to the Courant–Friedrichs–Lewy (CFL) stability condition. The insect and human-head grids contained 318 × 724 ×217 cells (approximately 50 million) and 510 × 474 × 539 cells (approximately 130 million), respectively.

Duration sensitivity was evaluated from 5 to 60 periods for the insect model and from 5 to 40 periods for the human-head model. The insect P_{abs} at 60 periods differed by 0.43% from the 15-period result. For the human head, the results from 15 to 40 periods remained within 0.29% of the 30-period reference. Production simulations therefore used 15 periods for the insect model and 30 periods for the human-head model.

E. RT to FDTD Workflow

The coupling between the RT analysis in Sionna and the full-wave simulations in Sim4Life followed a four-step workflow (see Fig. 2).

This field-to-dosimetry coupling follows the same general rationale as hybrid exposure-assessment workflows in which field quantities are first estimated and then used as excitation for full-wave dosimetry models [45], [46], [47].

1) Step 1–Extraction and Selection of Multipath Components: For each TX–RX and TX–RIS–RX pairing, Sionna returned the complete extracted multipath set, which was ranked in descending order of path gain. The strongest path was always retained. Each subsequent path was retained when its gain was within 10 dB of the previously retained path, up to a maximum of five paths. The five-path limit was introduced to keep the number of simultaneous plane-wave sources in each FDTD simulation computationally manageable.

The effect of this truncation was evaluated at all 440 RX positions by comparing the coherent gain calculated from the retained path set with that obtained from the complete extracted path set. For the RIS-assisted directional case, the median absolute difference was 0.049 dB and the 95th-percentile difference was 0.992 dB. For the direct-LoS reference, the corresponding differences were 1.247 and 5.594 dB, while for the isotropic-TX/no-RIS case they were 0.556 and 6.195 dB, respectively. The five-path limit therefore introduced only a small difference for most RX positions in the main RIS-assisted case, although larger differences occurred at some positions in the reference cases and were included in the sensitivity and uncertainty assessment.

The extracted coherent path gain $G_{\mathrm{path},i}$ includes the selected TX radiation pattern (isotropic or TR 38.901 array) and the propagation effects modeled by Sionna RT, with isotropic reception at the RX.

2) Step 2—FDTD Simulation With Coherent Superposition of Retained Paths: Full-wave simulations were performed in Sim4Life v9.0 (ZMT Zurich MedTech, Switzerland). For each RX snapshot, the retained multipath components were modeled in a single FDTD simulation by superposing multiple plane-wave excitations. For each path i, incidence angles (θ_i, ϕ_i) obtained from Sionna were applied directly in the FDTD excitation, consistent with the ray directions arriving at the RX/source region [see Fig. 1(c)] and the RT-to-FDTD workflow (see Fig. 2), using vertical linear polarization consistent with the TX polarization.

Each retained RT component was represented locally at the RX position by a plane-wave excitation. Across all extracted paths, the minimum distance between the RX and the final interaction point was 0.942 m, corresponding to approximately 82 wavelengths at 26 GHz. For the strongest path at each RX, the minimum distance was 1.073 m and the median distance was 10.06 m. The strongest components were therefore not generated by objects located immediately next to the phantom.

Propagation delays were not implemented as time-domain shifts, since doing so would require prohibitively long excitation windows. Instead, each path delay τ_i was converted into an equivalent phase offset

$$\psi_i = 2\pi f \tau_i \tag{1}$$

valid under the narrowband steady-state assumption at 26 GHz. The plane waves were combined coherently by assigning each excitation its phase offset ψ_i.

For numerical convenience, the excitation amplitudes were normalized such that the maximum resulting plane-wave root-mean-square (rms) amplitude equals 1 V/m, while preserving the relative amplitudes across paths.

Each plane-wave source i was assigned an rms amplitude proportional to the field estimate from Step 3, i.e., $E^{\mathrm{sim}}_{i,\mathrm{rms}} = E_{i,\mathrm{rms}}/E_{0,\mathrm{rms}}$, so that $\max_i E^{\mathrm{sim}}_{i,\mathrm{rms}} = 1$ V/m (rms). Key simulation parameters are summarized in Table I.

3) Step 3—Map Path Gain to Incident Field (Isotropic RX Reference): For each retained path i, Sionna provides the coherent power gain $G_{\mathrm{path},i}$ for an isotropic (1 × 1) receiver. The received power captured by the isotropic RX is

$$P_{\mathrm{rx},i} = P_{\mathrm{tx}}\, G_{\mathrm{path},i} \tag{2}$$

where P_{tx} is in watts.

To map $P_{\mathrm{rx},i}$ to an equivalent incident plane wave at the phantom location, we compute the IPD S_i using the effective

TABLE I
SUMMARY OF KEY PARAMETERS USED IN THE RT TO FDTD WORKFLOW

Category	Parameter	Value / Description
Greenhouse geometry and materials		
Domain size	Dimensions	$75 \times 75 \times 10$ m
Vegetation model	Tomato canopy	Homogeneous dielectric
Permittivity (26 GHz)	$(\varepsilon_r', \varepsilon_r'')$	$(15.0, 7.0)$
Material model (Sionna)	Foliage scattering	Lambertian pattern, $S = 0.3$
Sionna ray-tracing parameters		
Carrier frequency	f	26 GHz
Bandwidth	B	200 MHz
TX power	P_{tx}	20 dBm
RX model	–	Isotropic (1×1)
TX modes	–	Isotropic (0 dBi peak); 4×4 array (TR 38.901 element $\approx$8 dBi + array factor $\approx$12 dB $\Rightarrow$ $\approx$20 dBi peak), beam steered toward the (active) RIS; LoS reference: same array placed at RIS location and steered toward the RX.
RIS model	30×30 elements	$\lambda/2$ spacing, ideal phase-only reflection
Multipath selection rule	Iterative 10 dB threshold	Retain 1–5 strongest paths
Extracted quantities	Per path	AoA (θ_i, ϕ_i), delay τ_i, gain $G_{\text{path},i}$
Path interactions	Maximum path depth	8 propagation interactions per path
FDTD (Sim4Life) parameters		
Excitation	Plane waves	Superposition of 1–5 components per RX; normalized so $\max_i E_{i,\text{rms}} =$ 1 V/m (RMS)
Delay handling	Phase shift	$\psi_i = 2\pi f \tau_i$
Polarization	Linear	Vertical, consistent with TX
Grid resolution	Δ	0.08 mm (insect), 1 mm (human)
Simulation region	Source box	$40 \times 40 \times 40$ mm^3 (insect), $300 \times 300 \times 300$ mm^3 (human)
Insect phantom	*Bombus terrestris*	Flying posture, homogeneous tissue
Human phantom	IXI Heads V1.0	Tissue properties from IT'IS database
Outputs (normalized)	–	Insect $P_{\text{abs}}^{\text{FDTD}}$; Human $\text{APD}_{4\text{cm}^2}^{\text{FDTD}}$
Field mapping and scaling		
Received power	$P_{\text{rx},i}$	$P_{\text{tx}}\, G_{\text{path},i}$
Isotropic aperture	A_{iso}	$\lambda^2/(4\pi)$
IPD	S_i	$P_{\text{rx},i}/A_{\text{iso}}$
Field amplitude (RMS)	$E_{i,\text{rms}}$	$\sqrt{\eta_0 S_i}$
Max field (RMS)	$E_{0,\text{rms}}$	$\max_i E_{i,\text{rms}}$
Final scaling	–	$P_{\text{abs}}^{\text{real}} = E_{0,\text{rms}}^2\, P_{\text{abs}}^{\text{FDTD}}$; $\text{APD}_{4\text{cm}^2}^{\text{real}} = E_{0,\text{rms}}^2\, \text{APD}_{4\text{cm}^2}^{\text{FDTD}}$

aperture of an isotropic receiver

$$A_{\text{iso}} = \frac{\lambda^2}{4\pi}, \qquad S_i = \frac{P_{\text{rx},i}}{A_{\text{iso}}}. \tag{3}$$

This provides an equivalent free-space plane-wave representation of the retained path at the phantom location, expressed through the isotropic effective aperture, and is used here as a computational bridge between RT path gains and full-wave excitation amplitudes [27], [28], [29].

Assuming a plane wave in free space, the corresponding *rms* electric-field amplitude is

$$E_{i,\text{rms}} = \sqrt{\eta_0 S_i} \tag{4}$$

where η_0 is the free-space wave impedance.

4) Step 4—Scaling of Normalized FDTD Outputs: For numerical convenience, the multiplane-wave excitation in Sim4Life was normalized such that the maximum *rms* amplitude across the retained paths equals 1 V/m. Let $E_{0,\text{rms}} = \max_i E_{i,\text{rms}}$ denote the physical maximum rms amplitude for that RX snapshot. Since absorbed quantities scale with $|E|^2$, the normalized FDTD outputs are converted to physical levels as

$$P_{\text{abs}}^{\text{real}} = E_{0,\text{rms}}^2\, P_{\text{abs}}^{\text{FDTD}}, \qquad \text{APD}_{4\text{cm}^2}^{\text{real}} = E_{0,\text{rms}}^2\, \text{APD}_{4\text{cm}^2}^{\text{FDTD}}. \tag{5}$$

F. Exposure Metrics and Reference Quantities

Exposure was evaluated using two metrics suited to different body scales. For the human head, $\text{APD}_{4\text{cm}^2}$ denotes the peak absorbed power density averaged over a contiguous square 4 cm^2 region of the exposed skin surface. This corresponds to the absorbed power density quantity S_{ab} used in the international commission on non-ionizing radiation protection (ICNIRP) 2020 local basic restrictions, rather than to IPD. Sim4Life calculates this absorbed quantity directly; no conversion from incident to absorbed power density was applied.

At 26 GHz, the ICNIRP 2020 local basic restrictions for S_{ab} are 20 W/m^2 for general-public exposure and 100 W/m^2 for occupational exposure, averaged over 6 min and over a square 4 cm^2 body-surface area [12]. The general-public restriction was used for the main comparison because a greenhouse may be accessible to visitors, tourists, customers, bystanders, and workers who are not exposed under controlled occupational conditions. The occupational restriction applies to adults exposed under controlled conditions who are informed and trained about the applicable radiofrequency (RF) exposure risks. This may include trained technical staff, installers, maintenance personnel, researchers, farmers, or greenhouse workers when those controlled occupational conditions are satisfied.

The simulations represent steady-state narrowband exposure. For comparison with the ICNIRP restriction, each snapshot was conservatively treated as if the simulated field level were maintained over the full 6-min averaging period.

For the bumblebee model, total absorbed power (P_{abs}) was reported because averaging over 4 cm^2 is not meaningful at insect scale and insect-specific protection criteria are not established [12], [37]. The reported absorbed quantities can be scaled to other transmit powers by the square of the incident electric-field amplitude, or linearly with IPD, as described in Section II-E.

G. Sensitivity and Uncertainty Considerations

Sensitivity was evaluated separately for the RT, RT–FDTD coupling, and FDTD stages.

For the RT stage, the number of ray samples, random seed, and maximum path depth were varied. With 4×10^6 ray samples, all 440 RX positions had at least one path above the user-defined -300 dB postprocessing threshold. Across five random seeds, the median coherent gain varied by 0.77 dB. Increasing the maximum path depth from 8 to 10 changed the global median coherent gain by 0.34 dB. In the isotropic case, the position-specific absolute differences had a median of 3.01 dB and a 95th percentile of 15.90 dB.

For the RT–FDTD coupling, retaining the five strongest paths in the RIS-assisted directional case produced a median absolute coherent-gain difference of 0.049 dB and a 95th-percentile difference of 0.992 dB relative to the complete RT path set. The effect on the absorbed quantities was evaluated by comparing the $K = 5$ and $K = 10$ retained-path sets with $K = 20$ as the FDTD reference. For $K = 5$, the maximum absolute differences in the dominant and isotropic cases were 1.46% and 18.84%, respectively, for insect P_{abs}, and 1.71% and 19.93% for human $\text{APD}_{4\,\text{cm}^2}$. For $K = 10$, the corresponding differences decreased to 0.81% and 6.30% for the insect model and 0.76% and 6.90% for the human-head model.

For the FDTD stage, grid-resolution sensitivity was evaluated for both phantoms. The maximum mean difference was $2.84\% \pm 0.57\%$ for insect P_{abs} and $2.75\% \pm 0.68\%$ for human $\text{APD}_{4\,\text{cm}^2}$. The insect simulation-duration effect was 0.43% between the 15- and 60-period simulations. For the human-head model, the results from 15 to 40 periods remained within 0.29% of the 30-period reference, and the 30- and 40-period results differed by 0.02%.

For the homogeneous insect model, varying ε_r and σ independently by $\pm 50\%$ changed P_{abs} from -18.1% to +8.3%. A separate dielectric-property sweep was not performed for the human head because the heterogeneous phantom uses tissue-specific, frequency-dependent properties from the IT'IS database.

III. Results and Discussion

A. Propagation Results and Implications for Exposure

We first compare four propagation scenarios to quantify how vegetation blockage, transmit directivity, and RIS-assisted reflections reshape the coherent channel gain inside the greenhouse: (A) isotropic TX without RIS (baseline), (B) isotropic TX with RIS, (C) directional 4×4 TX with RIS, and (D) a directional TX placed at the RIS location (LoS reference).

In the baseline (A), no receiver has LoS due to vegetation blockage. Propagation is therefore dominated by diffuse foliage-induced components. The mean coherent channel gain is -122.1 dB, with deep fades below -160 dB. For $P_{\text{tx}} = 20$ dBm, a 200 MHz bandwidth, and a 10 dB noise figure, the noise power is approximately -81 dBm. The corresponding mean and median signal-to-noise ratios (SNRs) are -21.1 and -18.4 dB, respectively, confirming operation in a noise-limited regime.

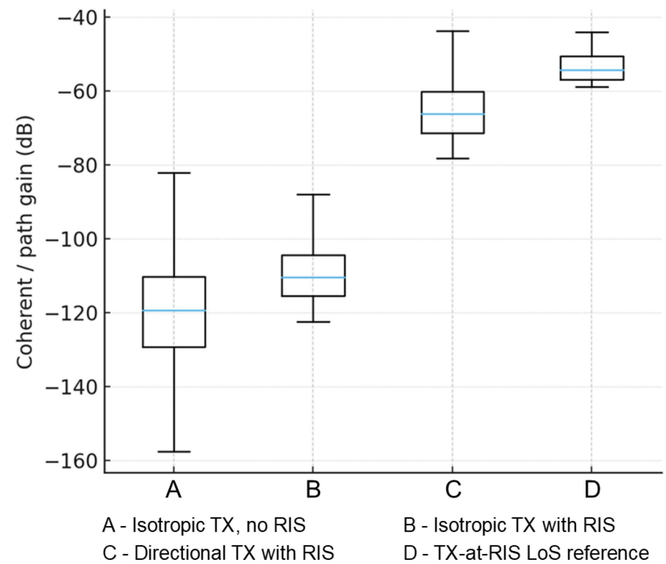

Fig. 3. Boxplot comparison of the coherent path-gain distributions in decibels across the four propagation scenarios defined in the legend. Outliers are omitted for visual clarity. Isotropic illumination provides only modest RIS-assisted improvement, whereas directional illumination enables coherent RIS-assisted propagation approaching the TX-at-RIS LoS reference.

Adding the RIS under isotropic illumination (B) yields only modest improvement. The mean coherent gain increases from -122.1 dB to -109.3 dB (median -119.4 dB to -110.4 dB), i.e., $\approx$12.7 dB on average, but the distribution remains broad. This behavior is consistent with weak and spatially inconsistent illumination of the RIS aperture, which reduces effective coherent reradiation.

In contrast, when the RIS is illuminated by the directional 4×4 TX (C), the gain distribution shifts upward and becomes markedly more stable. The mean coherent gain improves to -65.2 dB (median -66.3 dB), corresponding to $\approx$56.9 dB improvement relative to the isotropic baseline (A). The central 90% interval tightens to approximately $[-76, -50]$ dB, indicating a dominant and more deterministic TX–RIS–RX contribution. The LoS reference (D) provides an upper bound with mean -53.2 dB; the average gap between (C) and (D) is 12 dB, showing that, under strong illumination, the RIS can recover most of the benefit of a direct LoS-like link.

These propagation results provide the physical basis for the exposure trends reported next: isotropic illumination yields low incident field levels dominated by diffuse multipath, whereas RIS-assisted directional illumination strengthens a dominant component and produces strong location-dependent optimized gains at selected RX positions. The coherent path-gain distributions for the four propagation scenarios are compared in Fig. 3.

The observed scenario ordering is consistent with prior studies showing that exposure-relevant field levels depend strongly on deployment geometry, source directivity, and the degree of deterministic coupling in the propagation channel, rather than only on transmitted power [25], [29], [32]. In particular, the present results support the view that field-shaping mechanisms can increase local peak levels by strengthening dominant components, while the effect remains spatially dependent and closely tied to illumination efficiency of the reflecting structure [8], [9], [27].

To quantify the spatial variability of the evaluated propagation conditions, the peak-to-spatial-average coherent-gain ratios were 19.85, 21.12, and 16.20 dB for the isotropic-TX/no-RIS, isotropic-TX/RIS, and directional-TX/RIS scenarios, respectively. The corresponding numbers of RX positions within 3 dB of the maximum were 4, 3, and 4, while the P_{95} adjacent-location variations were 9.18, 9.25, and 8.46 dB/m. The two isotropic configurations reached their maximum at B11, 9.2 m from the TX, whereas the directional-TX/RIS configuration reached its maximum at F11, 19.9 m from the TX. Because the RIS configuration was optimized independently for each RX, these metrics characterize location-dependent optimized links rather than one simultaneous field distribution or physical hotspot area.

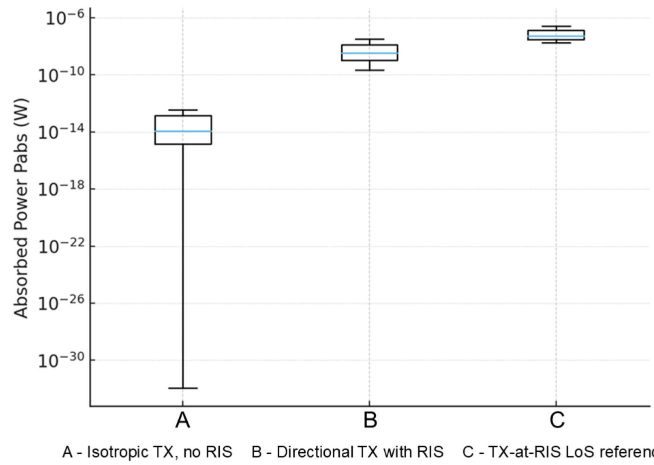

Fig. 4. Boxplot comparison of total insect absorbed power, P_{abs}, in watts across the three illumination scenarios defined in the legend. The vertical axis is shown on a logarithmic scale.

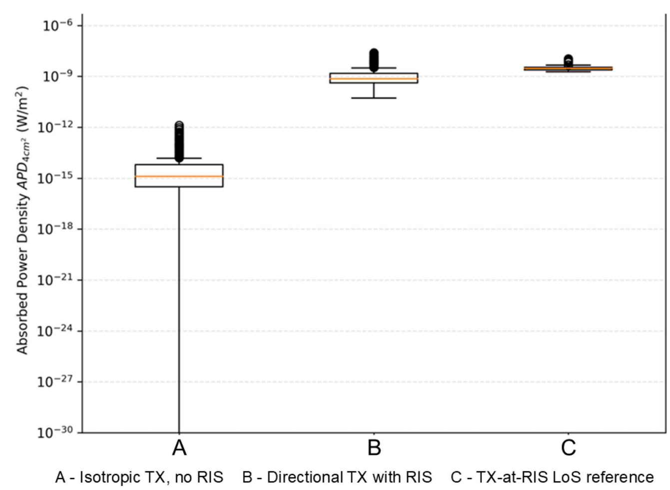

Fig. 5. Boxplot comparison of the human-head absorbed power density averaged over 4 cm^2, APD$_{4\text{cm}^2}$, in W/m^2 across the three illumination scenarios defined in the legend. The vertical axis is shown on a logarithmic scale.

B. Exposure Results: Insect and Human Metrics

Exposure simulations were performed for the isotropic baseline, the optimized RIS-assisted directional configuration [RIS (M-RX/P-RX)], and the LoS reference. The constrained RIS (M-Fix/P-RX) and RIS (M-Fix/P-Fix) configurations were evaluated at the RT stage only and were not propagated to FDTD. The isotropic-TX/RIS case was also not propagated to FDTD because its propagation gains remained close to the weak-field, diffuse regime and did not alter the qualitative exposure ordering relative to the baseline.

Insect absorbed Power: Across the three illumination scenarios, insect absorption spans several orders of magnitude. In the isotropic baseline, absorbed power is extremely small (median 1.2×10^{-14} W; mean 1.5×10^{-12} W; maximum 1.8×10^{-10} W), consistent with the weak and diffuse fields observed in the propagation results. Under RIS-assisted directional illumination, P_{abs} increases markedly: most values fall in the 10^{-10}–10^{-8} W range (mean 2.92×10^{-8} W; median 3.07×10^{-9} W), with a maximum of 1.5×10^{-6} W for the strongest optimized RX condition. The LoS reference yields P_{abs} in the 10^{-8}–10^{-7} W range (mean 1.9×10^{-7} W), providing an upper bound benchmark without vegetation blockage.

These results show that RIS-assisted field control does not uniformly increase absorption across the greenhouse; instead, it produces substantial location-to-location variation under the independently optimized RX conditions (see Fig. 4).

The strong spatial variability of P_{abs} in the RIS-assisted case is consistent with previous insect dosimetry studies showing that absorbed power in small flying insects is highly sensitive to incident field level, frequency, and body geometry [34], [35], [48]. In contrast to human exposure assessment, these values should be interpreted as dosimetric indicators rather than compliance quantities, since insect-specific protection criteria are not currently established [37].

Human Exposure (APD$_{4cm^2}$): Human exposure follows the same scenario ordering as the propagation results: the isotropic case yields the lowest APD, RIS-assisted directional illumination yields higher APD due to the strengthened dominant component, and the LoS reference produces the highest APD among the three scenarios (see Fig. 5).

The peak APD$_{4\text{cm}^2}$ remained below 10^{-4} W/m^2 in every scenario. Compared with the ICNIRP 2020 general-public local basic restriction of 20 W/m^2, this corresponds to a margin greater than 2×10^5, or more than 53 dB, under the conservative assumption that the simulated steady-state field level is maintained throughout the full 6-min averaging period [12]. The results indicate that configurations, which increase deterministic coupling (directionality and RIS focusing), increase local surface exposure, but the increase varies among RX-specific optimized conditions rather than occurring uniformly across locations.

In all cases, absorption is confined to superficial tissues (primarily skin), which is consistent with the shallow penetration depth at mmWave frequencies and with recent dosimetry studies on head and nonplanar body models using APD/IPD- based assessment above 6 GHz [14], [15], [18], [19]. The observed increase in APD_{4cm^2} under RIS-assisted directional illumination is also consistent with the broader finding that local surface metrics are strongly affected by field incidence conditions and metric definition when dominant components are present [16], [17].

Although the LoS reference yields the highest path gain and exposure, the RIS-assisted directional case recovers most of the propagation benefit (within 12.0 dB on average) while producing lower absorbed metrics, indicating a favorable connectivity-to-exposure tradeoff relative to this upper bound direct-illumination benchmark.

C. Limitations and Assessment Sensitivities

The FDTD exposure results correspond to the optimized RIS (M-RX/P-RX) configuration and should therefore be interpreted as an idealized upper bound for RIS-assisted coupling and field localization within the considered RIS configurations. This case assumes perfect geometric knowledge and separate mechanical orientation and electronic phase optimization for every RX, while the RIS is modeled as an ideal phase-only reflector with unit amplitude and no reflection losses or mutual coupling.

To evaluate more constrained operation, additional RT simulations were performed using fixed mechanical and electronic configurations. The median coherent path gain decreased from -66.30 dB for RIS (M-RX/P-RX) to -76.00 dB for RIS (M-Fix/P-RX) and -106.00 dB for RIS (M-Fix/P-Fix). The corresponding mean gains were -65.20, -75.84, and -105.00 dB, respectively. Thus, fixing the mechanical orientation reduced the median gain by 9.70 dB, while fixing both the mechanical orientation and the phase profile reduced it by 39.70 dB relative to the optimized configuration. These results confirm that the per-RX configuration used in the exposure analysis systematically maximizes RIS-assisted coupling. Because the constrained configurations were evaluated only at the RT stage, their detailed absorbed-power and absorbed-power-density distributions were not calculated. Vegetation dielectric properties and structural variability introduce uncertainty in absolute path gains and field levels; however, the relative ranking for propagation (isotropic $\ll$ isotropic+RIS$\ll$ RIS-assisted directional$\ll$ TX-at-RIS reference) is expected to be robust. Exposure was evaluated for isotropic, RIS-assisted directional, and TX-at-RIS reference only. In addition, mapping RT outputs to full-wave simulations relies on truncating the multipath set (10 dB rule). While this reduces computation, it may underestimate or overestimate local maxima depending on the coherence of discarded components. Future work will incorporate measurement validation in real greenhouse sections and will evaluate the impact of RIS nonidealities (reflection loss, phase errors, and finite control resolution) on both link enhancement and the spatial distribution produced by fixed or practically constrained RIS configurations.

These uncertainty sources are consistent with those commonly reported in exposure-assessment studies, where geometric variability, source modeling, and material parameters dominate the uncertainty budget [31]. Future validation with in situ measurements will also be important to assess the extent to which the simulated spatial gain patterns persist under nonideal hardware and environmental variability [33].

D. Relation to Previous Exposure-Assessment Studies

Compared with previous exposure-assessment studies in indoor deployments, the present work extends the analysis to a vegetation-dense greenhouse environment, where blockage and scattering strongly reduce deterministic coupling unless RIS- assisted directional illumination is used [25], [32]. The main contribution is not a new exposure metric, but a coupled propagation-to-dosimetry workflow that quantifies how RIS-enabled field shaping modifies both human surface exposure (APD_{4cm^2}) and insect absorbed power under the same channel realizations. This joint reporting is particularly relevant in greenhouse scenarios, where human compliance assessment and nonhuman dosimetric evaluation may be required simultaneously [14], [37].

IV. Conclusion

We presented a hybrid RT-to-FDTD framework to jointly assess mmWave propagation and exposure assisted by a RIS in a realistic tomato greenhouse at 26 GHz. Dense vegetation produced a weak diffuse baseline, with a mean coherent channel gain of approximately -122 dB. Directional illumination of the RIS increased the mean coherent channel gain by approximately 56.9 dB and approached the LoS upper bound reference.

Under receiver-specific optimized conditions, surface assistance increased exposure by different amounts across the evaluated receiver locations. For the *Bombus terrestris* model, absorbed power increased from typical baseline values of 10^{-14}–10^{-12} W to 10^{-10}–10^{-8} W under directional surface-assisted illumination, with a maximum of 1.5×10^{-6}W for the strongest optimized receiver condition. For the human-head phantom, the absorbed power density averaged over 4 cm^2 remained below 10^{-4} W/m^2, more than 53 dB below the 2020 general-public local basic restriction of the International Commission on Nonionizing Radiation Protection.

Compared with the LoS upper bound reference, the surface-assisted directional configuration retained much of the propagation benefit while producing lower dosimetric quantities, indicating a favorable connectivity-to-exposure tradeoff in the considered greenhouse layout. Future work will include nonideal surface behavior and measurement validation in real greenhouse sections.

References

[1] A. Soumya, C. Krishna Mohan, and L. R. Cenkeramaddi, "Recent advances in mmWave-radar-based sensing, its applications, and machine learning techniques: A review," *Sensors*, vol. 23, no. 21, 2023, Art. no. 8901.

[2] S. Nie et al., "mmWave on a farm: Channel modeling for wireless agricultural networks at broadband millimeter-wave frequency," in *Proc. 19th Annu. IEEE Int. Conf. Sens., Commun., Netw.*, 2022, pp. 388–396.

[3] F. K. Schwering, E. J. Violette, and R. H. Espeland, "Millimeter-wave propagation in vegetation: Experiments and theory," *IEEE Trans. Geosci. Remote Sens.*, vol. 26, no. 3, pp. 355–367, Mar. 1988.

[4] D. Lee, O. Ozdemir, A. Ram, and I. Guvenc, "Analysis and prediction of coverage and channel rank for UAV networks in rural scenarios with foliage," *IEEE Open J. Veh. Technol.*, vol. 6, pp. 1943–1962, 2025. [Online]. Available: https://ieeexplore.ieee.org/document/11066253/

[5] E. J. S. D. León, O. F. Á. Herrera, E. S. A. L. Ávila, D. O. B. Goñzalez, and E. S. R. R. Rodriguez, "Deployment of private 5G networks in greenhouses: 26 GHz propagation modeling and comparison with 3GPP standards," in *Proc. 2024 IEEE 1st Latin Amer. Conf. Antennas Propag.*, 2024, pp. 1–2.

[6] D. Cama-Pinto et al., "Empirical model of radio wave propagation in the presence of vegetation inside greenhouses using regularized regressions," *Sensors*, vol. 20, no. 22, 2020, Art. no. 6621.

[7] H. Radpour, M. Hofer, and T. Zemen, "Adaptive RIS control for mobile mmWave NLoS communication using single-bit feedback," in *Proc. IEEE Wireless Commun. Netw. Conf. Workshops*, 2026, pp. 1–6.

[8] D.-T. Phan-Huy, Y. Bénédic, S. H. Gonzalez, and P. Ratajczak, "Creating and operating areas with reduced electromagnetic field exposure thanks to reconfigurable intelligent surfaces," in *Proc. IEEE 23rd Int. Workshop Signal Process. Adv. Wireless Commun.*, 2022, pp. 1–5.

[9] H. L. dos Santos, C. J. Vaca-Rubio, R. Kotaba, Y. Song, T. Abrao, and P. Popovski, "EMF exposure mitigation in RIS-assisted multi-beam communications," 2023, *arXiv:2305.05229*.

[10] H. Ibraiwish, A. Elzanaty, Y. H. Al-Badarneh, and M.-S. Alouini, "EMF-aware cellular networks in RIS-assisted environments," *IEEE Commun. Lett.*, vol. 26, no. 1, pp. 123–127, Jan. 2021.

[11] S. Alekseev, A. Radzievsky, M. Logani, and M. Ziskin, "Millimeter wave dosimetry of human skin," *Bioelectromagnetics*, vol. 29, no. 1, pp. 65–70, 2008.

[12] International Commission on Non-Ionizing Radiation Protection (ICNIRP), "Guidelines for limiting exposure to electromagnetic fields (100 kHz to 300 GHz)," *Health Phys.*, vol. 118, no. 5, pp. 483–524, 2020.

[13] *IEEE Standard for Safety Levels With Respect to Human Exposure to Electric, Magnetic, and Electromagnetic Fields, 0 Hz to 300 GHz*, IEEE Standard C 95.1, 2019.

[14] A. Hirata, "Assessment of human exposure to electromagnetic fields: Review and future directions," *IEEE Trans. Electromagn. Compat.*, vol. 63, no. 5, pp. 1619–1630, May 2021.

[15] Y. Diao and A. Hirata, "Effect of incidence angle on the spatial-average of incident power density," *IEEE Trans. Electromagn. Compat.*, vol. 63, no. 5, pp. 1709–1716, May 2021.

[16] S. S. Zhekov, M. Yao, C. Di Paola, B. Xu, and S. Zhang, "A study on EMF exposure assessments with different metrics for user equipment antennas at 6 and 10 GHz," *IEEE Trans. Electromagn. Compat.*, vol. 66, no. 1, pp. 61–69, Jan. 2024.

[17] M. Yao, G. F. Pedersen, and S. Zhang, "Investigation of criterion for applying incident power density in the near-field region for EMF assessment at quasi-millimeter and millimeter-wave frequencies," *IEEE Trans. Electromagn. Compat.*, vol. 66, no. 3, pp. 706–719, Mar. 2024.

[18] Y. Diao and A. Hirata, "FDTD assessment of exposures to far-field mmWave beams in anatomical head model," *IEEE Trans. Electromagn. Compat.*, vol. 65, no. 5, pp. 1282–1291, May 2023.

[19] D. Kapetanović et al., "Assessment of incident power density on spherical head model up to 100 GHz," *IEEE Trans. Electromagn. Compat.*, vol. 64, no. 5, pp. 1296–1303, Oct. 2022.

[20] Y. Diao, E. A. Rashed, and A. Hirata, "Assessment of absorbed power density and temperature rise for nonplanar body model under electromagnetic exposure above 6 GHz," *Phys. Med. Biol.*, vol. 65, 2020, Art. no. 224001.

[21] Y. Wang, S. Safavi-Naeini, and S. K. Chaudhuri, "A hybrid technique based on combining ray tracing and FDTD methods for site-specific modeling of indoor radio wave propagation," *IEEE Trans. Antennas Propag.*, vol. 48, no. 5, pp. 743–754, May 2000.

[22] S. Shikhantsov et al., "Hybrid ray-tracing/FDTD method for human exposure evaluation of a massive MIMO technology in an industrial indoor environment," *IEEE Access*, vol. 7, pp. 21020–21031, 2019.

[23] R. Wydaeghe, S. Shikhantsov, G. Vermeeren, L. Martens, E. Tanghe, and W. Joseph, "Hybrid ray-tracing-QuaDRiGa/FDTD method for realistic 28 GHz exposure with 6G CF-MaMIMO in 3D outdoor environments," npj *Wireless Technol.*, vol. 2, 2026, Art. no. 13.

[24] S. Shikhantsov et al., "Massive MIMO propagation modeling with user-induced coupling effects using ray-tracing and FDTD," *IEEE J. Sel. Areas Commun.*, vol. 38, no. 9, pp. 1955–1963, Sep. 2020.

[25] S. Shikhantsov, A. Thielens, G. Vermeeren, P. Demeester, L. Martens, and W. Joseph, "Numerical assessment of human EMF exposure to collocated and distributed massive MIMO deployments in an industrial indoor environment," *IEEE Trans. Electromagn. Compat.*, vol. 65, no. 4, pp. 960–971, Apr. 2023.

[26] R. Wydaeghe et al., "Realistic human exposure at 3.5 GHz and 28 GHz for distributed and collocated MaMIMO in indoor environments using hybrid ray-tracing and FDTD," *IEEE Access*, vol. 10, pp. 130996–131004, 2022.

[27] K. Omi, D. Funahashi, and A. Hirata, "Performance analysis of incident power density evaluation by inverse source method," *IEEE Trans. Electromagn. Compat.*, vol. 63, no. 5, pp. 1649–1657, May 2021.

[28] C. Li et al., "Efficient evaluation of incident power density by millimeter-wave MIMO user equipment," *IEEE Trans. Electromagn. Compat.*, vol. 65, no. 4, pp. 1090–1097, Apr. 2023.

[29] O.-S. Kwon et al., "Estimation of power density radiated from radio base station for telecommunication services," *IEEE Trans. Electromagn. Compat.*, vol. 63, no. 2, pp. 384–389, Feb. 2021.

[30] R. Cicchetti et al., "Estimation of the peak power density in the vicinity of cellular and radio base station antennas," *IEEE Trans. Electromagn. Compat.*, vol. 46, no. 2, pp. 275–290, Feb. 2004.

[31] B.-C. Kim et al., "Uncertainty estimation for evaluating human exposure levels to RF electromagnetic fields from cellular base stations," *IEEE Trans. Electromagn. Compat.*, vol. 54, no. 2, pp. 246–253, Feb. 2012.

[32] S. S. Zhekov and B. Xu, "Evaluation of EMF exposure from distributed MIMO antennas for 6G in an industrial indoor environment," *IEEE Trans. Electromagn. Compat.*, vol. 67, no. 2, pp. 403–417, Feb. 2025.

[33] D. Colombi et al., "Methods and practices for in situ measurements of RF EMF exposure from 5G millimeter wave base stations," *IEEE Trans. Electromagn. Compat.*, vol. 64, no. 6, pp. 1986–1993, Jun. 2022.

[34] A. Thielens, D. Bell, D. B. Mortimore, M. K. Greco, L. Martens, and W. Joseph, "Exposure of insects to radio-frequency electromagnetic fields from 2 to 120 GHz," *Sci. Rep.*, vol. 8, 2018, Art. no. 3924.

[35] A. Thielens, M. K. Greco, L. Verloock, L. Martens, and W. Joseph, "Radiofrequency electromagnetic field exposure of Western honey bees," *Sci. Rep.*, vol. 10, no. 1, 2020, Art. no. 461.

[36] E. De Borre et al., "Radio-frequency exposure of the yellow fever mosquito (*A. aegypti*) from 2 to 240 GHz," *PLoS Comput. Biol.*, vol. 17, no. 10, 2021, Art. no. e1009460.

[37] A. Thill, M.-C. Cammaerts, and A. Balmori, "Biological effects of electromagnetic fields on insects: A systematic review and meta-analysis," *Rev. Environ. Health*, vol. 39, no. 4, pp. 853–869, 2024.

[38] F. Aït Aoudia, J. Hoydis, M. Nimier-David, S. Cammerer, and A. Keller, "Sionna RT: Technical report," 2025, *arXiv:2504.21719*.

[39] 5 GCM, "5G channel model for bands up to 100 GHz," 5GCM, White Paper Version 2.3, Oct. 2016. [Online]. Available: https://www.5gworkshops.com/5GCMSIG_White\%20Paper_r2dot3.pdf

[40] V. Degli-Esposti, E. M. Vitucci, M. Di Renzo, and S. Tretyakov, "Reradiation and scattering from a reconfigurable intelligent surface: A general macroscopic model," *IEEE Trans. Antennas Propag.*, vol. 70, no. 10, pp. 8691–8706, Oct. 2022.

[41] E. M. Vitucci, M. Albani, S. Kodra, M. Barbiroli, and V. Degli-Esposti, "An efficient ray-based modeling approach for scattering from reconfigurable intelligent surfaces," *IEEE Trans. Antennas Propag.*, vol. 72, no. 3, pp. 2673–2685, Mar. 2024.

[42] Y. Kano, "CC0 bumblebee," Sketchfab, 2020, 3D model obtained via photogrammetry. licensed under CC0 public domain. [Online]. Available: https://sketchfab.com/3d-models/cc0-bumblebee-f0aac424f44b48cf92 17ffe126ace5ca

[43] A. Proksch et al., "Perspectives terahertz honey bee sensing," *Sci. Rep.*, vol. 15, no. 1, 2025, Art. no. 10638.

[44] IT'IS Foundation, "IXI heads v1.0," in *Virtual Population—Regional Human Models*, 2024, release date: 18 Jun. 2024. [Online]. Available: https://itis.swiss/virtual-population/regional-human-models/ixi-heads/ixi-heads-v1-0/

[45] Y. Diao and A. Hirata, "Hybrid computational method for determining incident power density and specific absorption rate for human exposure assessment to electromagnetic fields from 1 to 30 GHz," *IEEE Trans. Electromagn. Compat.*, vol. 63, no. 5, pp. 1690–1698, May 2021.

[46] K. Kiminami et al., "Novel specific absorption rate (SAR) estimation method based on 2-D scanned electric fields," *IEEE Trans. Electromagn. Compat.*, vol. 50, no. 4, pp. 828–836, Apr. 2008.

[47] D. Colombi et al., "Efficient whole-body SAR assessments by means of surface scan measurements," *IEEE Trans. Electromagn. Compat.*, vol. 56, no. 3, pp. 539–548, Mar. 2014.

[48] C. Toribio, A. Thielens, L. Verloock, L. Martens, G. Vermeeren, and W. Joseph, "Near field radio-frequency electromagnetic field exposure of a Western honey bee," *IEEE Trans. Antennas Propag.*, vol. 70, no. 2, pp. 1320–1327, Feb. 2022.